

Machine Learning Phases of Strongly Correlated Fermions

Kelvin Ch'ng,¹ Juan Carrasquilla,² Roger G. Melko,^{2,3} and Ehsan Khatami¹

¹*Department of Physics and Astronomy, San José State University, San José, CA 95192, USA*

²*Perimeter Institute for Theoretical Physics, Waterloo, Ontario N2L 2Y5, Canada*

³*Department of Physics and Astronomy, University of Waterloo, Ontario N2L 3G1, Canada*

Machine learning offers an unprecedented perspective for the problem of classifying phases in condensed matter physics. We employ neural network machine learning techniques to distinguish finite-temperature phases of the strongly-correlated fermions on cubic lattices. We show that a three-dimensional convolutional network trained on auxiliary field configurations produced by quantum Monte Carlo simulations of the Hubbard model can correctly predict the magnetic phase diagram of the model at the average density of one (half filling). We then use the network, trained at half filling, to explore the trend in the transition temperature as the system is doped away from half filling. This transfer learning approach predicts that the instability to the magnetic phase extends to this region, albeit with a transition temperature that falls rapidly as a function of doping. Our results pave the way for other machine learning applications in correlated quantum many-body systems.

The various modern architectures of neural networks consisting of multiple layers and neuron types (see Fig. 1 for an example) can be “trained” to classify, with a high degree of accuracy, intricate sets of labeled data [1]. The data, e.g, a series of handwritten digits, are fed to the network input layer and the outcome, read at the output layer, are neuron activations corresponding to the different digits. Common to most algorithms involving neural networks is the training procedure, which is an optimization problem where the free parameters associated with connections between neurons in adjacent layers and their biases (additive constants) are slowly adjusted until a high classification accuracy is attained. Embodied in the study of quantum and classical statistical mechanics are the many-body states, which can be understood as immense data sets associated with the equilibrium state of the system, and over which machine learning techniques can be naturally applied. Early applications of machine learning ideas in condensed matter physics focused on their connection to renormalization group methods [2], obtaining the Green’s function of the Anderson impurity model [3], categorizing real materials [4–7], or learning ground states and thermodynamics of many-body systems [8, 9]. Tensor-network representations of quantum states have also been recently proposed as a powerful tool for supervised learning [10].

Recently, neural network machine learning algorithms have been successfully adopted to distinguish phases of matter in classical Ising-type models, effectively locating critical temperatures at which transitions between phases take place [11, 12]. Two of the authors found that using a simple network consisting of only one hidden layer one, can predict the transition temperature with up to 99% accuracy for two-dimensional (2D) Ising models, solely based on spin configurations generated by a Monte Carlo simulations and in the absence of any information about the underlying lattice or the order parameter.

The extension of the technique to quantum mechanical

systems is less straightforward, as the quantum Monte Carlo simulations of interacting particles involve an additional dimension associated with imaginary time in the path integral formalism at finite temperatures, or the projection parameter for ground state calculations; quantum fluctuations can distort the easily recognizable picture of spin configurations in the ordered phase of the classical system, and therefore, significantly affect the training accuracy of the neural network. Here, using quantum Monte Carlo simulations of the Hubbard model of strongly-correlated fermions on cubic lattices

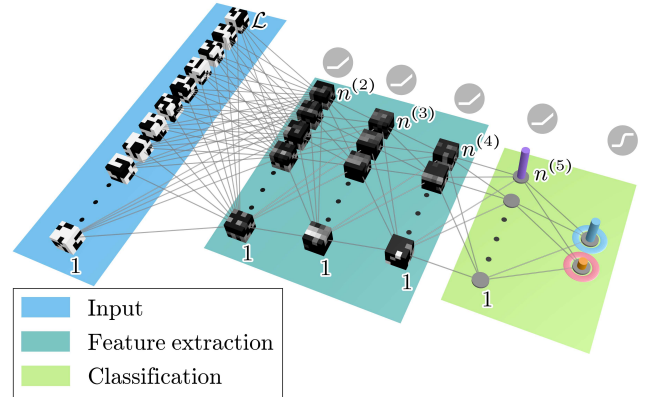


FIG. 1. Schematic diagram of the 3D convolution neural network used to obtain T_N for the half-filled 3D Hubbard model. The input are the auxiliary field configurations in a four-dimensional grid; three spatial dimensions of size 4 (total of $N = 4^3$ sites), and one imaginary time dimension of size $\mathcal{L} = 200$. Numbers of volumetric feature maps in the hidden feature extraction layers are, $n^{(2)} = 32$, $n^{(3)} = 16$, and $n^{(4)} = 8$. $n^{(5)} = 8$ in the fully-connected layer. During training, dropout regularization with a rate of 0.5 was used to mitigate overtraining. To classify the input system as ordered or unordered, each of the 8 fully-connected neurons is then connected to each of the two readout neurons using softmax function as a neural activation function. The output neuron with the highest probability represents the activated neuron.

and convolutional neural networks (CNNs), we show that one can successfully classify finite-temperature phases of quantum systems and estimate transition temperatures with a reasonable degree of accuracy on relatively small lattice sizes.

The Fermi-Hubbard Hamiltonian [13, 14] in the particle-hole invariant form is expressed as

$$H = -t \sum_{\langle ij \rangle \sigma} c_{i\sigma}^\dagger c_{j\sigma} + U \sum_i (n_{i\uparrow} - \frac{1}{2})(n_{i\downarrow} - \frac{1}{2}) - \mu \sum_{i\sigma} n_{i\sigma}, \quad (1)$$

where $c_{i\sigma}$ ($c_{i\sigma}^\dagger$) annihilates (creates) a fermion with spin σ on site i , $n_{i\sigma} = c_{i\sigma}^\dagger c_{i\sigma}$ is the number operator, U is the onsite Coulomb interaction, $\langle \dots \rangle$ denotes nearest neighbors, t is the corresponding hopping integral, and μ is the chemical potential. $\mu = 0$ corresponds to the half-filled model (average density of one fermion per site, $n = 1$). We set $t = 1$ as the unit of energy, and consider the model on three-dimensional (3D) cubic lattices.

The 3D model at half filling realizes a finite-temperature transition to the antiferromagnetic Néel phase for any $U > 0$, analogous to the magnetic ordering in the 2D classical Ising model. The transition temperature, T_N , which is relatively well known from the analysis of the staggered spin structure factor, or the staggered susceptibility [15, 20–22, 25–27], is a non-monotonic function of the interaction strength; it increases rapidly with increasing U in the weak-coupling regime ($U \lesssim 8$), a result that can be captured using the random phase approximation [15], and decreases at large U . In the strong-coupling regime ($U \gtrsim 12$), the half-filled model can be effectively described by the antiferromagnetic (AFM) Heisenberg model, whose exchange constant, and hence, Néel temperature, is proportional to $1/U$ [16].

Our goal here is to train a CNN to identify finite-temperature phase boundaries of the Hubbard model. We utilize the determinantal quantum Monte Carlo (DQMC) [17], which reduces the numerical evaluation of the observables of the Fermi-Hubbard model to a stochastic averaging over a set of discrete auxiliary fields extending in space and along an *imaginary time* dimension. The spin correlations of the model can be written directly in terms of the correlations in our particularly chosen auxiliary field [18], rendering it an obvious choice to be used in the identification of magnetic phases through machine learning, although a previous attempt including two of the authors has not been successful [19]. The training is done using the field configurations generated during DQMC simulations in a range of temperatures around one or two critical points. The objective is to use the trained network to map out the entire phase boundary associated with the same critical phenomenon by varying the parameters driving the transition and generating “test” data sets of the field configurations. In this work, we focus on the magnetic

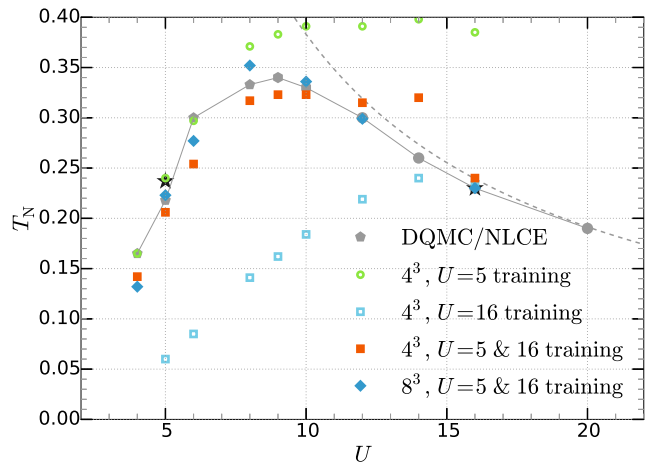


FIG. 2. Prediction of the Néel transition temperature by the neural network. Using the auxiliary spin configurations, the network is trained separately at $U = 5$ and $U = 16$ for $N = 4^3$, and simultaneously at $U = 5$ and 16 for $N = 4^3$ and $N = 8^3$. The critical temperatures used for the training of the network with $N = 4^3$ are shown as stars (see text). Grey filled symbols are the estimates for T_N in the thermodynamic limit from DQMC and NLCE simulations. Grey pentagons, hexagons and circles are taken from Refs. 20, 21, and 22, respectively. The dashed line shows the asymptotic behavior for T_N at large U ($3.83/U$). The solid line is a guide to the eye.

properties of the Hubbard model.

We use a 3D CNN, originally developed for human action recognition in videos [23], implemented in Tensorflow [24]. Convolutions are designed to return information about spatial dimension and locality to the simpler idea of a fully-connected feed-forward neural network. In our case, the three spatial dimensions of the cubic lattice are treated with the convolution, while slices in the fourth imaginary time axis are used as different filter channels [1]. A schematic picture of the network is shown in Fig. 1. We use 3 or 4 hidden layers, depending on the spatial size of the system, for feature extraction followed by a fully connected layer before the output layer [18]. The optimal number of neurons in each layer (resulting in the largest accuracy) is found using a Monte Carlo optimization procedure [18].

To benchmark our results and validate our approach, we start with the 3D Hubbard model at half filling and explore the accuracy with which we can predict the Néel phase boundary in the temperature-interaction space. We train the network to distinguish (by activating the corresponding output neuron) spin configurations belonging to the ordered phase ($T < T_N$) from those of the unordered high-temperature phase. The approximately 80,000 labeled configurations at various temperatures around T_N are generated through DQMC simulations for two interactions strengths, $U = 5$ and 16, one in the weak-coupling and one in the strong-coupling regime,

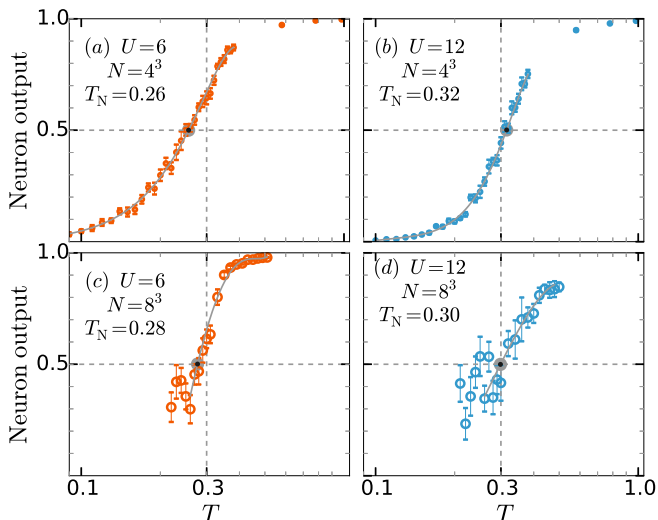


FIG. 3. Average output of the neuron that is trained to be activated in the unordered phase as a function of temperature at half filling. The network is maximally confused (average is 0.5) at the transition temperatures. We use 90,000 configurations for $N = 4^3$ (top row) and 10,000 configurations for $N = 8^3$ (bottom row). The grey solid lines are fits to data in the ranges shown. The vertical dashed lines indicate the estimates for T_N in the thermodynamic limit (~ 0.30 for both U values) from other studies (see caption of Fig. 2).

and shuffled before use in the training. The trained network is then used to classify other configurations as the temperature is varied across the estimated critical values for other values of U between 5 and 16.

The results for two system sizes $N = 4^3$ and $N = 8^3$ are shown in Fig. 2 as full squares and diamonds. They demonstrate that despite notable disagreements at some values of U , remarkably, the network can predict the non-trivial shape of the phase boundary with reasonable degree of accuracy even with a system size of $N = 4^3$. We obtain similar results by increasing the linear system size by a factor of two ($N = 8^3$). Figure 2 also summarizes T_N in the thermodynamic limit from recent unbiased studies [20–22]. Note that T_N is not well defined for finite clusters, which can lead to uncertainties in the labeling of the configurations in the training process. However, the *exact* value of T_N is, in principle, not required for the training. One can omit configurations from the training data in an arbitrary temperature range in the proximity of the estimated critical value, e. g., the temperature at which the correlations reach the linear size of the cluster, at the expense of losing some predicting accuracy by the network after the training. Here, we take advantage of the fact that finite-size errors are small in the strong-coupling regime and use $T_N = 0.23$ for $U = 16$, obtained for the thermodynamic limit [22], for both cluster sizes. For $U = 5$, however, we use the approximate critical temperatures $T_N = 0.24$ and 0.25 for $N = 4^3$ and 8^3 , respectively, from the analysis of the Binder ratio for the

order parameter [20].

The predicted critical temperatures for other values of U during the classification are taken as temperatures at which the network is maximally “confused”, i.e. when the average output crosses 0.5. Figure 3 shows the average output of the neuron, in the classification, that is trained to be activated, that is, to return 1, in the ordered phase. Results are shown for the two system sizes and for $U = 6$ and 12. We perform the classifications on 90,000 (10,000) configurations per temperature for $N = 4^3$ ($N = 8^3$). The data become noisier with smaller number of configurations for the larger system and by increasing U , and so, we use fits to a third degree polynomial using data near the 0.5 crossing to better T_N .

The simultaneous use of configurations for $U = 5$ and 16 is crucial in obtaining the results in Fig. 2. We find that a network that is trained to distinguish phases only in the weak-coupling regime, e.g., for $U = 5$, correctly predicts the trend in T_N vs U for systems in the weak-coupling regime, but grossly overestimates it for systems in the intermediate and strong-coupling regimes. Similarly, a network that is trained with configurations only for $U = 16$, underestimates T_N for any $U < 16$ (see the open symbols in Fig. 2). Physically, this can be understood as follows: The transition to the AFM ordered phase is less sharp in the weak-coupling regime with substantial double occupancy still present in the system above the transition. As a result, the network that is trained only in this regime, tracks the onset of Mott physics, which moves to higher temperatures as the interaction strength increases, not the Néel transition. On the other hand, the network that is trained only in the strong-coupling regime, tracks the onset of the region with significantly reduced double occupancy and stronger AFM correlations, which takes place at lower temperatures for smaller values of U . The competition between these two scenarios when training with both $U = 5$ and $U = 16$ data is encoded in our network and manifests itself in the significant overestimation of T_N at $U = 14$ and the underestimation of T_N in the weak-coupling regime (see Fig. 2).

Does the magnetically-ordered phase survive if we dope the system away from half filling, and if so, what is the dependence of T_N on doping? We set to answer these questions for $U = 9$, where the transition temperature is highest at half filling. We train the network using spin configurations obtained for $U = 9$ at half filling and then classify other configurations generated at different $T (< T_N$ at $n = 1$) as we decrease the chemical potential from zero in the DQMC simulations. As soon as μ deviates from zero, the configuration weight in the DQMC can become negative, leading to the so-called “sign problem” [28]. We treat the neuron output as a (binary) physical observable, which, like spin correlations, can be written as a nonlinear function of the auxiliary spins [18], with an expectation value that is

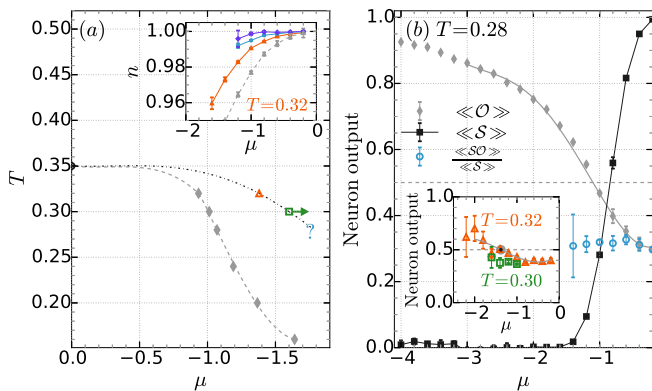


FIG. 4. (a) Magnetic phase diagram of the 3D Hubbard model away from half filling for $U = 9$. Empty color (filled grey) symbols are estimates for the Néel temperatures, with (without) taking the minus sign problem into account, obtained from a neural network that is trained to identify the phase at half filling. Lines are guides to the eye. Inset: equations of state (density vs μ) for $U = 9$ at $T = 0.24, 0.28$, and 0.32 (solid lines from top to bottom, respectively). The grey dashed line is calculated without taking the sign problem into account at $T = 0.32$. (b) Average neuron output calculated with and without considering the sign problem in the DQMC at $T = 0.28$. The grey solid line is a fit to data near the 0.5 crossing point. Inset: $\langle SO \rangle / \langle S \rangle$ at $T = 0.32$ and 0.30 vs μ . Solid line is the fit to estimate T_N at $T = 0.32$.

calculated in the conventional way by including the sign in the averaging and dividing by the average sign, typical for DQMC [18]. This procedure is valid as long as the average sign does not vanish.

The results are summarized in Fig. 4(a), where we show the dependence of T_N on μ . Similarly to half filling, T_N is estimated as the temperature the average neuron output crosses 0.5. To note the effect of the negative sign problem on our results, we also show the average neuron output if the sign is ignored during the calculation of the expectation value (grey filled points). Regardless, the transition temperature remains nonzero at $n \neq 1$, but rapidly decreases as soon as $\mu < -1.0$. The flat region at $\mu > -1.0$ is a direct consequence of the Mott physics near half filling setting in. However, at the temperatures we have access to, the Mott gap is not fully developed yet, and the density starts deviating from 1 around $\mu = -1.0$.

This is more clearly seen in the equations of state shown in the inset of Fig. 4(a) at $T = 0.24, 0.28$ and 0.32 . They also show that, for example, at $T = 0.32$ and $\mu = -1.4$, which is approximately the onset of the Néel phase, the density is $n \sim 0.97$. The equation of state at $T = 0.32$ sets a lower bound of ~ 0.96 also for the density at the transition point when $T = 0.30$. The actual density is likely closer to $n = 0.97$. These observations are consistent with results from other more conventional methods [22], and show that, even though the critical μ decreases rapidly by decreasing the temperature, the opening of the Mott gap is keeping the critical density

very close to unity. In Fig. 4(b), we show the average neuron output with and without taking the sign problem into account vs μ at $T = 0.28$. We also show the average of the sign itself. As the latter approaches zero around $\mu = -1.5$, the accuracy in the expectation value of the neuron output is largely compromised.

Figure 4(a) also shows that ignoring the sign problem leads to an underestimation of T_N at a given chemical potential. However, it also leads to a smaller average density at a given μ (see the grey dashed line in the inset). One may wonder if *two wrongs can make a right* in this case; will the magnetic phase diagram in the temperature-density space be the same regardless of whether or not we take the sign problem into account? The answer to this question may be relevant to a recent suggestion that the sign problem can be circumvented using networks trained in sign problematic regions [19]. Note that here, we are “transfer learning” by applying our network, trained on the sign-problem-free parameter region, to the sign problematic region, an approach that can potentially be taken to track down the onset of the pseudogap phase in the 2D Hubbard model away from half filling.

At $T = 0.32$, the critical density corresponding to the critical $\mu = -0.9$ [see diamonds in Figure 4(a)] is $n \sim 0.98$ according to the equation of state obtained by ignoring the sign problem. Even though this value seems significantly different from $n \sim 0.97$ obtained with taking the sign problem into account, we cannot rule out an agreement given the uncertainties associated with the estimation of T_N from the 0.5 crossing of neuron outputs. At lower T , lack of reliable data due to the sign problem prevents us from performing a similar comparison.

We have utilized neural network machine learning techniques to predict the onset of the finite-temperature magnetically ordered phases of the 3D Fermi-Hubbard model. We train a 3D CNN using auxiliary spin configurations for a range of temperatures around the transition temperature, sampled over during DQMC simulations of two systems in the weak- and strong-coupling regimes. We show that the trend in the Néel temperature of the half-filled model as a function of the interaction strength can be captured by using the trained network to classify configurations generated for other interaction strengths. We then train a network at half filling for $U = 9$ and use it to predict the fate of the ordered phase as the system is doped away from half filling. We find that the instability persists in the latter region, however, in a close proximity of the commensurate filling.

Acknowledgements We acknowledge useful conversations with Rajiv R. P. Singh, Andy Millis, Simon Trebst, and Peter Broecker. R.M. acknowledges support from NSERC and the Canada Research Chair program. Additional support was provided by the Perimeter Institute for Theoretical Physics. Research at

Perimeter Institute is supported by the Government of Canada through the Department of Innovation, Science and Economic Development Canada and by the Province of Ontario through the Ministry of Research, Innovation and Science.

- [29] V. I. Iglovikov, E. Khatami, and R. T. Scalettar, Phys. Rev. B **92**, 045110 (2015).
 [30] J. E. Hirsch, Phys. Rev. B **28**, 4059 (1983).
 [31] J. E. Hirsch, Phys. Rev. B **34**, 3216 (1986).
 [32] <http://quest.ucdavis.edu/> and <https://code.google.com/p/quest-qmc>.

-
- [1] M. A. Nielsen, *Neural Networks and Deep Learning* (Determination Press, 2015).
 [2] P. Mehta and D. J. Schwab, (Unpublished) preprint: arXiv:1410.3831 (2014).
 [3] L.-F. Arsenault, A. Lopez-Bezanilla, O. A. von Lilienfeld, and A. J. Millis, Phys. Rev. B **90**, 155136 (2014).
 [4] A. G. Kusne, T. Gao, A. Mehta, L. Ke, M. C. Nguyen, K.-M. Ho, V. Antropov, C.-Z. Wang, M. J. Kramer, C. Long, and I. Takeuchi, Sci Rep **4**, 6367 (2014), 25220062[pmid].
 [5] S. V. Kalinin, B. G. Sumpter, and R. K. Archibald, Nat Mater **14**, 973 (2015), progress Article.
 [6] L. M. Ghiringhelli, J. Vybiral, S. V. Levchenko, C. Draxl, and M. Scheffler, Phys. Rev. Lett. **114**, 105503 (2015).
 [7] S. S. Schoenholz, E. D. Cubuk, D. M. Sussman, E. Kaxiras, and A. J. Liu, Nat Phys **12**, 469 (2016), letter.
 [8] G. Carleo and M. Troyer, arXiv:1606.02318.
 [9] G. Torlai and R. G. Melko, arXiv:1606.02718.
 [10] E. M. Stoudenmire and D. J. Schwab, arXiv:1605.05775.
 [11] J. Carrasquilla and R. G. Melko, (Unpublished) preprint: arXiv:1605.01735 (2016).
 [12] L. Wang, arXiv:1606.00318.
 [13] N. F. Mott, Proceedings of the Physical Society. Section A **62**, 416 (1949).
 [14] J. Hubbard, Proceedings of the Royal Society of London A: Mathematical, Physical and Engineering Sciences **276**, 238 (1963).
 [15] R. T. Scalettar, D. J. Scalapino, R. L. Sugar, and D. Toussaint, Phys. Rev. B **39**, 4711 (1989).
 [16] A. W. Sandvik, Phys. Rev. Lett. **80**, 5196 (1998).
 [17] R. Blankenbecler, D. J. Scalapino, and R. L. Sugar, Phys. Rev. D **24**, 2278 (1981).
 [18] S. supplementary material at ..., .
 [19] P. Broecker, J. Carrasquilla, R. G. Melko, and S. Trebst, (Unpublished) preprint: arXiv:1608.07848 (2016).
 [20] E. Kozik, E. Burovski, V. W. Scarola, and M. Troyer, Phys. Rev. B **87**, 205102 (2013).
 [21] T. Paiva, Y. L. Loh, M. Randeria, R. T. Scalettar, and N. Trivedi, Phys. Rev. Lett. **107**, 086401 (2011).
 [22] E. Khatami, Preprint: arXiv:cond-mat/1603.02681 (2016).
 [23] S. Ji, W. Xu, M. Yang, and K. Yu, IEEE Transactions on Pattern Analysis and Machine Intelligence **35**, 221 (2013).
 [24] M. Abadi, *et al.*, TensorFlow: Large-scale machine learning on heterogeneous systems (2015). Software available from tensorflow.org.
 [25] R. Staudt, M. Dzierzawa, and A. Muramatsu, The European Physical Journal B - Condensed Matter and Complex Systems **17**, 411 (2000).
 [26] P. R. C. Kent, M. Jarrell, T. A. Maier, and T. Pruschke, Phys. Rev. B **72**, 060411 (2005).
 [27] D. Hirschmeier, H. Hafermann, E. Gull, A. I. Lichtenstein, and A. E. Antipov, Phys. Rev. B **92**, 144409 (2015).
 [28] E. Y. Loh, J. E. Gubernatis, R. T. Scalettar, S. R. White, D. J. Scalapino, and R. L. Sugar, Phys. Rev. B **41**, 9301 (1990).

Supplementary Materials: Machine Learning Phases of Strongly Correlated Fermions

Kelvin Ch'ng ¹, Juan Carrasquilla ², Roger G. Melko ^{2,3}, Ehsan Khatami ¹

¹*Department of Physics and Astronomy, San José State University, San José, CA 95192, USA*

²*Perimeter Institute for Theoretical Physics, Waterloo, Ontario N2L 2Y5, Canada*

³*Department of Physics and Astronomy, University of Waterloo, Ontario N2L 3G1, Canada*

Determinant quantum Monte Carlo

In the DQMC, the partition function $Z = \text{Tr}e^{-\beta H}$ is expressed as a path integral by discretizing the inverse temperature β into \mathcal{L} slices of length $\Delta\tau$. The one-body (kinetic) and two-body (interaction) terms of the Hubbard Hamiltonian (1) are then separated in each time slice, leading to a product of two exponentials: $Z = \text{Tr}(e^{-\Delta\tau K} e^{-\Delta\tau V})^{\mathcal{L}} + \mathcal{O}(\Delta\tau^2)$, where K and V are the kinetic and interaction parts of the Hamiltonian, respectively. Since the two terms do not commute, this process introduces a small controlled error of the order of $\Delta\tau^2$. The interaction terms at different times can then be written in terms of one-body (quadratic) fermion operators using the Hubbard-Stratonovich (HS) transformation

$$e^{-U\Delta\tau n_{\uparrow}n_{\downarrow}} = \frac{1}{2} e^{-U\Delta\tau(n_{\uparrow}+n_{\downarrow})/2} \sum_{s=\pm 1} e^{-s\lambda(n_{\uparrow}-n_{\downarrow})}, \quad (2)$$

where $\cosh \lambda = e^{U\Delta\tau/2}$, at the expense of introducing a sum over the field of auxiliary (spin) variables like s in a $D + 1$ -dimensional space (D spatial and 1 imaginary time). The fermionic degrees of freedom in the quadratic form can be integrated out analytically, resulting in the product of two determinants, one for each fermion species, and leaving behind the sum over the $2^{N\mathcal{L}}$ configurations of the auxiliary spins, where N is the spatial size of the system. Hence, the partition function can be expressed as

$$Z \propto \sum_{\{s_{i,l}\}} \det M_{\uparrow}(\{s_{i,l}\}) \det M_{\downarrow}(\{s_{i,l}\}), \quad (3)$$

where M_{σ} is a $N \times N$ matrix that depends on the spin configuration $\{s_{i,l}\}$, and i and l represent the spatial and time indices.

Observables are estimated by important sampling over the configurations, which is performed, e.g., using the Metropolis algorithm, with the product of determinants as the probability, to accept or reject proposed local changes to the field. However, the determinants are costly to update and, other than in few special cases, become negative at low temperatures, leading to the infamous ‘‘sign problem’’ [28, 29]. At half filling, the two determinants have the same sign by symmetry, and thus,

there is no sign problem. Away from half filling one can take the absolute value of the product of determinants as the new probability in the Metropolis algorithm, but have to treat the sign with the observable explicitly. The expectation value of a physical observable, O , can be calculated using

$$\langle O \rangle = \frac{\langle\langle SO \rangle\rangle}{\langle\langle S \rangle\rangle}, \quad (4)$$

where S denotes the of sign of the product of determinants and $\langle\langle \dots \rangle\rangle$ represents the Monte Carlo average using the absolute value of the product of determinants as the probability. Here, we take the neuron outputs as the observable.

The particular decoupling scheme we have chosen is especially useful for inferring magnetic ordering by the machine purely based on the auxiliary fields. This is because the correlations between fermionic spins S can be written in terms of auxiliary spins [30, 31]:

$$\langle S_i(\tau) S_j(0) \rangle = (1 - e^{-\Delta\tau U})^{-1} \langle s_i(\tau) s_j(0) \rangle. \quad (5)$$

Therefore, the auxiliary field variables are effectively representing the fermion spins with the same correlations in space and time. The decoupling can be done using other variables that couple to density or pairing operators, which can be more helpful in detecting other phases, including charge density wave or superconductivity. We do not explore those possibilities here.

We use the quantum electron simulation toolbox (QUEST) [32] for our DQMC simulations. The toolbox, with minimal modifications, allows for outputting of the HS field configurations at arbitrary intervals during the simulations. We use 1,000 (500) warmup sweeps and from 10,000 to 100,000 (1,000 to 10,000) measurement sweeps for $N = 4^3$ ($N = 8^3$) in each run. We repeat runs with different random number seeds to obtain the desired number of configurations. The HS field configuration is written into a file after every 10 sweeps, the same frequency typically used to perform physical measurements. For training, we choose the temperature grid for every value of U so that we have the same number of temperature points above and below the expected T_N . The temperatures are chosen in a nonuniform grid that

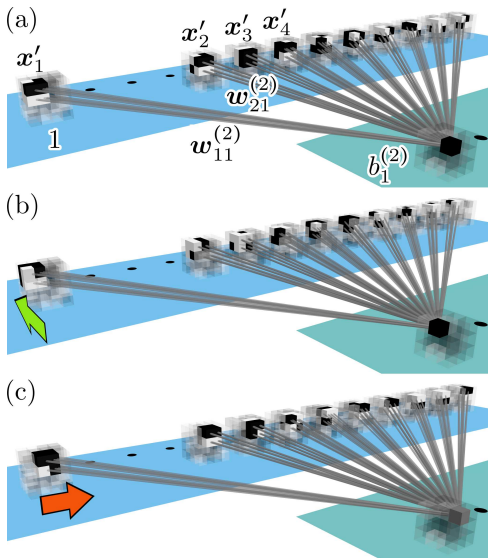


FIG. 5. The construction of volumetric feature maps is shown above. To produce the highlighted neuron in the volumetric feature map, from the input x_i , a shared filter $w_{i1}^{(2)}$ is convolved with a $2 \times 2 \times 2$ local receptive cube x'_i across all the inputs in the imaginary time slices, adding a bias offset $b_1^{(2)}$, before being activated using ReLU. Sliding the $2 \times 2 \times 2$ cube in each of the spatial dimension whilst repeating the convolution procedure completes a volumetric feature map. The spatial size of the volumetric feature map can be preserved by using zero-padding.

can extend from 0.03 to about 3.0 depending on U and N .

The discretization of the imaginary time interval $[0-\beta]$ ($\beta = 1/T$) in the DQMC introduces a systematic Trotter error, which scales like $\Delta\tau^2$, where $\Delta\tau = \beta/\mathcal{L}$ and \mathcal{L} is the number of time slices. Thus, in principle, one has to choose a variable \mathcal{L} at different temperatures so that the error in physical observables is of the same order. However, such configurations, with variable size of the fourth dimension, are not useful in the training of a network whose size of the input layer has to be kept fixed. Hence, we choose a large fixed $\mathcal{L} = 200$ for all β such that $\Delta\tau$ remains below the threshold value of $(8U)^{-1/2}$, where the Trotter error can be neglected, for the largest U values and the lowest temperatures considered here. Moreover, we are not interested in calculating physical observables, rather we are interested in locating the critical points at which the correlations of the system, both in the spatial and in the imaginary time dimensions, diverge, and so, the discretization errors can be essentially ignored.

The convolutional neural network (CNN)

Each auxiliary field configuration is fed into a 3D convolution neural network (CNN) with the different

imaginary time slices encoded as a different filter channel.

$$\text{CNN for } N = 4^3$$

For $N = 4^3$, each of the $4 \times 4 \times 4$ configurations from the \mathcal{L} imaginary time slices is immediately connected to 32 hidden volumetric feature maps for feature extraction and in order for the network to detect a collection of unique features.

To produce the volumetric feature maps in the first hidden layer, a shared filter (also known as kernel) $w_{lm}^{(2)}$ is convolved with a $2 \times 2 \times 2$ local receptive cube from each input and then offset with a shared bias $b_m^{(2)}$ followed by a rectified linear unit (ReLU) $f(z) = \max(0, z)$ as the neural activation function. As shown in Fig. 5, sliding the local receptive cube with stride of one collectively in each spatial dimension on the \mathcal{L} input cubes completes the construction of a volumetric feature map. Mathematically, a convolution procedure is the tensor product of the filter with the input plus a bias offset, $z = wx + b$. To preserve the input size after each convolution procedure so that the information around the border does not deplete too quickly as more convolution procedure is applied, especially with smaller input size, zero padding was used; each of the input cubes was padded with zero so that the volume is increased to $5 \times 5 \times 5$ and when a convolution procedure is performed, the output volume is the same as the input, i.e. $4 \times 4 \times 4$.

In order to make the neural network deeper, as deeper networks are typically more powerful, we use two more convolution layers with ReLU. 16 and 8 volumetric feature maps are used for the second and third hidden convolution layers, respectively. We repeat the procedure describe above to construct the feature maps in these layers.

The final feature extraction layer is connected to the classification layer for making judgement and categorizing the input. Each of the 64×8 individual neurons from the third feature extraction layer are connected to each of the 8 hidden fully-connected neurons for making abstract judgements. Finally, each of the 8 hidden neurons are connected to 2 output neurons using softmax as neural activation function with one of the output neuron representing the input configuration as being in the ordered state ($T < T_N$) and the other as in the unordered state ($T > T_N$). The output of the softmax function is given as a probability distribution estimating the likelihood of the correct output; as such, the sum of outputs from the two neurons is unity. As shown in Fig. 1, the activated output neuron is the one with the highest probability.

During training, dropout regularization with a dropout rate of 0.5 is used on the 8 fully-connected neuron for mitigating overfitting; that means, half of the 8 fully-connected neurons are temporarily deactivated at

random. This forces the neurons to adapt to more robust features.

An exponential decaying learning rate is also used to ensure that the network starts out learning rapidly and slows down the learning after the model is close to convergence. The learning rate is given by

$$\eta = \eta_0 \lambda^{\text{training epoch}}, \quad (6)$$

where the initial learning rate $\eta_0 = 10^{-3}$, and the decay rate $\lambda = 0.925$. A complete training epoch is defined as when the network has stepped through the whole set of training data once.

We use a cross-entropy cost function given by [1]

$$C = -\frac{1}{n_{\text{td}}} \sum_x \sum_{i=1}^2 [y_i \ln a_i + (1 - y_i) \ln(1 - a_i)], \quad (7)$$

where x is the input data and n_{td} is the number of training data. Figure 6 displays the cost function as training progresses. We use a batch size of 200 during the training.

CNN for $N = 8^3$

To keep the computational cost of the optimizations manageable, for the $N = 8^3$, we perform only valid convolutions (without zero-padding) with ReLU using 4 hidden feature extraction layers. To prevent overshooting the optimal model, a more aggressive decay rate $\lambda = 0.875$ was used.

Hand-picking the number of feature maps and fully-connected neurons, like for the case of $N = 4^3$, yields no learning. So, to avoiding a costly hyperparameter grid search, we perform a Monte Carlo sampling for 20 search iterations in the search space where each of the (even) number of feature maps and fully-connected neurons is constrained to the interval [8,128]. The optimized hyperparameters we found are $n^{(2)} = 54$, $n^{(3)} = 26$, $n^{(4)} = 14$, $n^{(5)} = 18$, and $n^{(6)} = 64$.

Training accuracy

Figure 6 shows the training progress of our networks in different cases vs training epochs. In a training epoch, we go through the entire set of shuffled training data once. %85 of the input data was used for training and %15 for testing. Test data is used as a gauge for overfitting (overtraining). The network overfits to the training data when the training accuracy continues to improve, but the testing accuracy stalls. We stop the training once we detect overfitting. The criterion is that the training accuracy and testing accuracy should not deviate for more than 10 successive training evaluation.

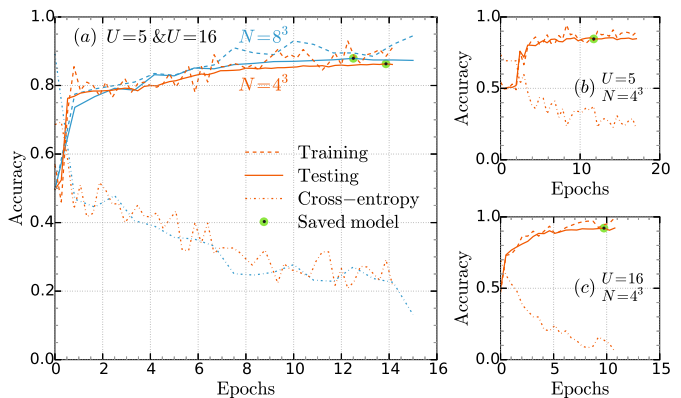


FIG. 6. Training accuracy for (a) simultaneous training with $U = 5$ and 16, (b) $U = 5$ alone, and (c) $U = 16$ alone, vs epochs.

As seen in Fig. 6, the algorithm saves the *best* model when the difference between training accuracy and testing accuracy is less than 2.5%, the training accuracy is greater than testing accuracy, and the current testing accuracy is better than the last recorded testing accuracy. The location of last saved models are shown as green circles for each case. The model is saved where the testing accuracies are %86.3 (%87.9) for $N = 4^3$ ($N = 8^3$) in Fig. 6(a), %84.6 in Fig. 6(b) and %92.1 in Fig. 6(c).